SNAP-SHOT MRI

Nobel Lecture, December 8, 2003

by

Peter Mansfield

Sir Peter Mansfield Magnetic Resonance Centre, Department of Physics and Astronomy, University of Nottingham, Nottingham, NG7 2RD, U.K.

INTRODUCTION

The topic of magnetic resonance imaging (MRI) started for us at Nottingham in the early summer of 1972. During a discussion with one of my graduate students, Peter Grannell and my post-doc Dr Allan Garroway, concerning multiple-pulse line narrowing experiments in solids, the idea occurred to me to use the line narrowing technique as a means of effectively removing dipolar interactions in a material like CaF_2 and at the same time impose an external linear gradient on the sample thus broadening the line shape to reveal the atomic or molecular structure within the sample.

It soon became apparent, however, even with the achievable narrowed linewidths of around 1 Hz for CaF_2, corresponding to a line width reduction of 3×10^4, that the residual line width was still too broad using practical external gradients to resolve the atomic structure in a single crystal of CaF_2. Despite this setback, work continued with artificial one-dimensional lattices made up of several thin plates of camphor.

Peter Grannell and I continued this work during the course of 1972 and it resulted finally in a paper presented at the First Specialized Colloque Ampère, Krakow in 1973 (1). Formal publication appeared shortly after (2). These papers emphasized the Fourier transform approach used, even though the images of the camphor stacks were one-dimensional. It was clear that we had made our task much more difficult by choosing to work with solids. Thoughts rapidly turned to liquid-like spin systems where the line narrowing approach would be unnecessary.

The imaging approach considered so far was essentially one or two-dimensional. The next step was to define a thin slice of material so that this would be imaged without spill over to adjacent planes. This was achieved using a technique called selective irradiation (3).

One of the major practical difficulties encountered with MRI to this point was the time it took to acquire the data. Line-scanning, for example, took typically 10–20 min to acquire an image comprising 64×64 pixels (4).

The breakthrough came in 1977 with the introduction of echo-planar imaging (EPI) (5). This snap-shot technique meant that in principle complete two-dimensional images could be achieved in extremely short times

ranging from 20–50 ms. However, to achieve these acquisition times, yet another inventive step was required. This was the introduction of active magnetic screening (6,7). Ordinary magnetic gradient coils, necessary to define the slice thickness and image axes, were found to interact strongly with the metal cryostat structure of the super-conductive magnet. Time dependent currents induced in these structures would decay away with their own independent time constant, adding an undesirable and unpredictable time dependence to the otherwise static magnetic field.

By actively shielding the gradient coils, all extraneous time dependence is obviated, together with all undesirable reflected static magnetic fields. Of course, the magnetic screening process itself introduces magnetic fields which change the character of the gradient field but in a well defined and calculable manner.

Magnetically screened gradient coils now form an integral part of virtually all commercial MRI scanners.

EXPERIMENTAL APPARATUS

Figure 1 shows a home built 0.5 T whole body MRI scanner together with a patient bed support. Figure 2 shows a doubly screened gradient coil assembly used in the experimental scanner of Figure 1. With a doubly screened gradient coil in which the primary coil comprises a single current loop, it can be shown that the unshielded loop carrying current I produces magnetic flux

Figure 1. Photograph of home built magnetic resonance imager based on a 0.5 T super-conductive magnet.

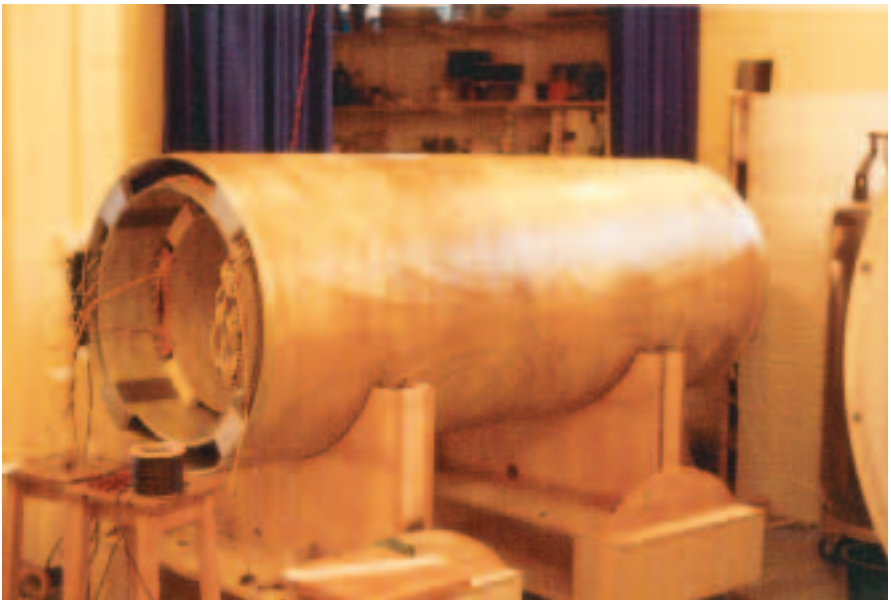

Figure 2. Photograph of a doubly screened active magnetic shielded gradient coil set for insertion in the super-conductive magnet of Figure 1.

lines which form a series of elliptic like magnetic field loops with displaced centres (7). However if the current loop or the primary coil is now magnetically screened with the double screen arrangement, the magnetic field lines within the inner screen are exactly the same as produced by the primary coil in free space. However, between the screens the magnetic flux is confined and the field inverts. The magnetic field at the center of the coil assembly takes the same form and magnitude as the unscreened coil. That is to say, the magnetic field B within a current loop is as expected for an unscreened loop. Outside the outer screen the field B = 0. If the inner magnetic screen is removed leaving the outer screen, flux confinement between the screens can no longer occur and the magnetic field now leaks beyond the outer screen.

ECHO-PLANAR IMAGING (EPI)

Imaging Sequence

The mathematical relationship between real-space and k-space, first described in 1750 by the French mathematician Joseph Fourier, is known as the Fourier transform (FT). It takes the general form

$$S(\mathbf{k}) = \int d\mathbf{r}\, \rho(\mathbf{r})\, \exp(i\mathbf{k}.\mathbf{r}) \qquad \text{Eq. [1]}$$

where

$$\mathbf{k} = \int_0^t \gamma \partial \mathbf{G}(t') / \partial t'\, dt' \qquad \text{Eq. [2]}$$

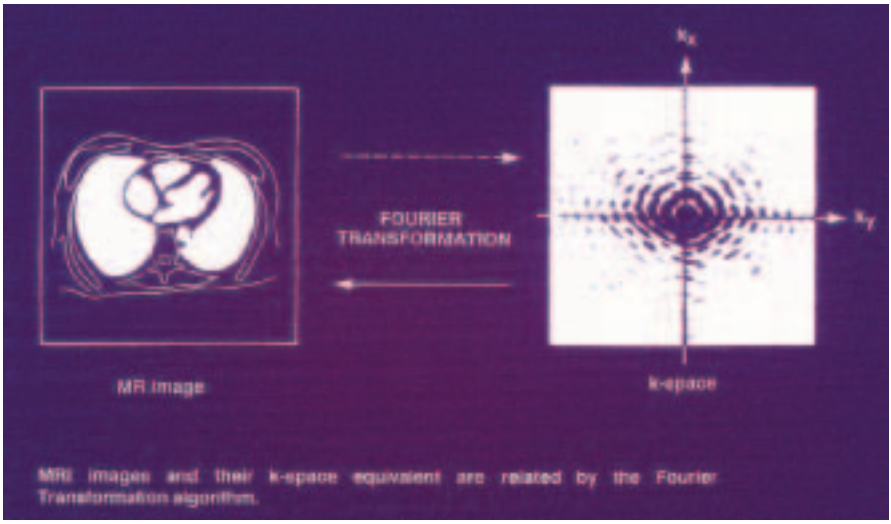

Figure 3. Diagram of a slice through the mediastinum showing the two lung fields and heart mass, also shown is the Fourier transform of this real-space image to the k-space map. (Reproduced with permission from M K Stehling, R Turner and P Mansfield, SCIENCE 253, 43–50 (1991).)

and where **k** and **r** may both be one-, two- or three-dimensional. The density $\rho(\mathbf{r})$ describes the image in real space and $S(\mathbf{k})$ describes the image in k-space. In our case $\mathbf{G}(t)$ is an externally applied time dependent magnetic gradient, γ is the magneto-gyric ratio which is constant for a particular nuclear spin species and t is the evolution time.

Using the Fourier transform expression in Eq. [1] allows a reversible transformation from k-space to real or r-space. This is exemplified in the forward and inverse Fourier transforms shown in Figure 3.

In fact the two dimensional k-space image is built up from a series of one dimensional free induction decays, (FID's), suitably stacked to give an image which is in effect the diffraction pattern of the object. The inverse FT of the k-space image produces the r-space image. In this case a transverse cross-sectional image through the mediastinum showing a diagram of the heart mass and lung fields.

In order to obtain the k-space map in a single experiment a specially designed pulse sequence is applied as shown in Figure 4. In general terms this comprises an initial spin preparation phase followed by a transverse slice selection pulse. This creates an active magnetic signal or FID which is allowed to decay away in the presence of the spatial encoding gradients G_x and G_y. For EPI these are applied in the form of a square wave or a trapezoidal waveform for G_y and either a long low level pulse or a train of short blipped pulses for G_x. In either case the areas under the long low pulse or the string of blips must be equal. The effect of these gradient waveforms causes the FID follow-

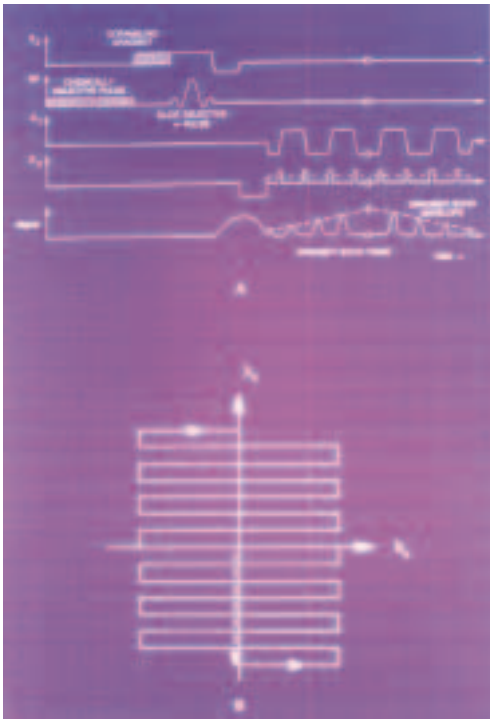

Figure 4. (Upper diagram) MBEST pulse sequence diagram and (lower diagram) k-space trajectory (Reproduced with permission from M K Stehling *et al.,* Brit J Radiol 63, 430–437 (1990).)

ing slice selection to dephase and rephase in a series of spin echoes. The amplitude of these spin echoes is initially low but grows to a maximum and then decays provided an initial dephasing gradient pulse is arranged immediately before the blipped or low level G_x sequence starts.

Also included in Figure 4 is the k-space trajectory. This starts at $k_x = k_y = 0$. The pre-pulse described above displaces the trajectory from 0 to $-k_{xmax}$ at which point the locus starts from $k_y = 0$ moving right to k_{ymax}. At this point the trajectory is displaced upwards with the first positive blip. The transverse scan then proceeds from right to left traversing the full k_y scan from k_{ymax} to $-k_{ymax}$. In this way the whole of the **k** plane is scanned. During this journey the signal is regularly sampled to produce the first step in obtaining the k-space scan as sketched in Figure 3. The remaining operation is an editing function which reverses the order of all data in alternate lines of the k-space image. At this point there are two options to choose from in order to produce the r-space image. The first is to perform a two-dimensional FT on the k-space map thereby producing the r-space image. However, to do this in general requires an overhead in time for data manipulation in addition to the two dimensional FT. The alternative approach is to take the first and last points in the reordered k-space scan and, metaphorically speaking, pull the whole array out, like a string of beads, to form a one dimensional array. The whole string is Fourier transformed using a one dimensional FT with less computing overhead.

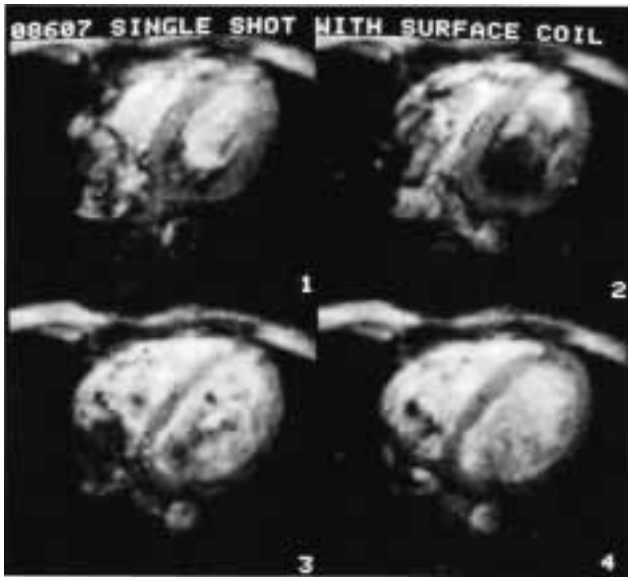

Figure 5. Snap-shot EPI images through the heart obtained with use of a surface coil. (1) Transection during systole shows left ventricular myocardial wall thickening. (2) Rapid ventricular filling in late systole. (3, 4) Transections obtained during diastole show thinner myocardial walls. The spatial resolution of these images is less then 2 mm. (Reproduced with permission from M J Stehling *et al.,* RADIOLOGY, 170: 257–263, (1989).)

General Two Dimensional Imaging Results at 0.5 T

The above described EPI sequence was used to image a series of patients and volunteers during the early eighties through to the nineties. Whole body scans may be performed comprising 64 transections commencing in the upper thorax and moving down the torso in 5 mm steps through the mediastinum, liver, kidney into the lower abdomen and finishing just below the bladder. They are an example of a quick sighting scan, the whole imaging process taking approximately one minute.

Figure 5 shows four EPI snap-shots taken through the heart using a surface coil on the chest wall (8). Each image is acquired at a different phase of the cardiac cycle. Figures 5.1 and 5.2, for example, correspond to different phases during systole, when the heart is in contraction and pumping. Figure 5.2 shows loss of signal (black) due to turbulence within the left ventricle. Figures 5.3 and 5.4 were acquired during the relaxed phase or diastole. In all images the myocardium gives a less intense signal allowing differentiation of the muscle tissue from blood.

Figure 6 shows four transections through the liver of a patient with a series of hydatid cystic lesions (9). These show as bright regions within the darker liver. An imaging variation on the same patient using the inversion-recovery or IR-EPI sequence uses an initial spin inversion pulse as the preparation phase. After a short delay or inversion time TI, the EPI sequence follows. When TI = 0 we have the normal sections as in Figure 6. By varying TI, short

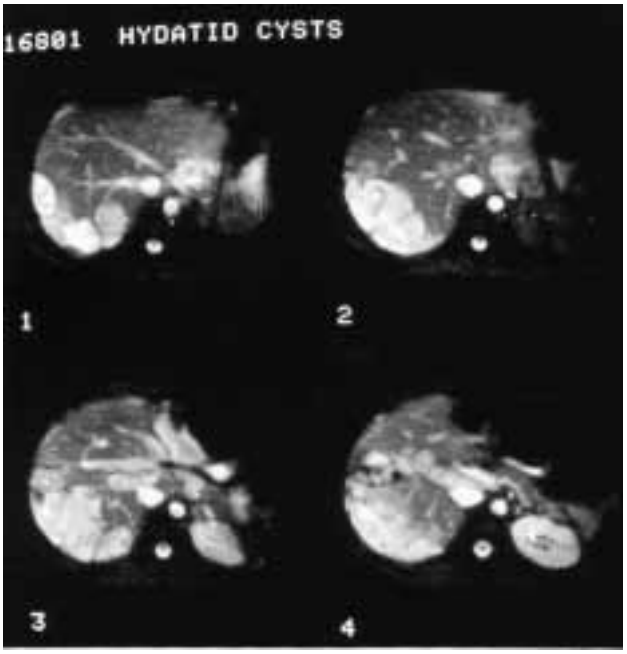

Figure 6. Four 128 ms acquisition time snap-shot MBEST images of a liver with hydatid cysts. These images are based on 128 × 128 pixel arrays with approximately 2.3 mm in-plane resolution. (Reproduced with permission from M J Stehling *et al.,* Brit J Radiol 63: 430–437 (1990).)

T_1 signal components within the image may be effectively removed thereby delineating the normal tissue. This procedure can be used to indicate clear margins between the lesions and the normal tissue. By increasing TI long relaxation time components may be eliminated thereby revealing the relatively fast relaxing hydatid cystic lesions.

Foetal Imaging Results at 0.5 T

An important area of application of EPI has been foetal imaging during the 3rd trimester. This has been valuable in assessing cases of foetal growth retardation (10–12).

Figure 7 shows a maternal coronal view of a foetal saggital section at 37 weeks gestation. The foetal section, taken from a set of scans, clearly shows the head, brain and spinal column and also the right leg. The darker signal from within the amniotic sac is the placenta. The brighter signal regions surrounding the foetus come from the amniotic fluid.

In other transectional images at 37 weeks gestation, highlighting of the lung field can be used to measure foetal lung volume. The same technique can be used to measure the subcutaneous fatty tissues surrounding the foetus.

Foetal birthweight versus the EPI estimated foetal volume has also been measured for 12 babies with birthweight spanning the range 1.5–3.5 kg

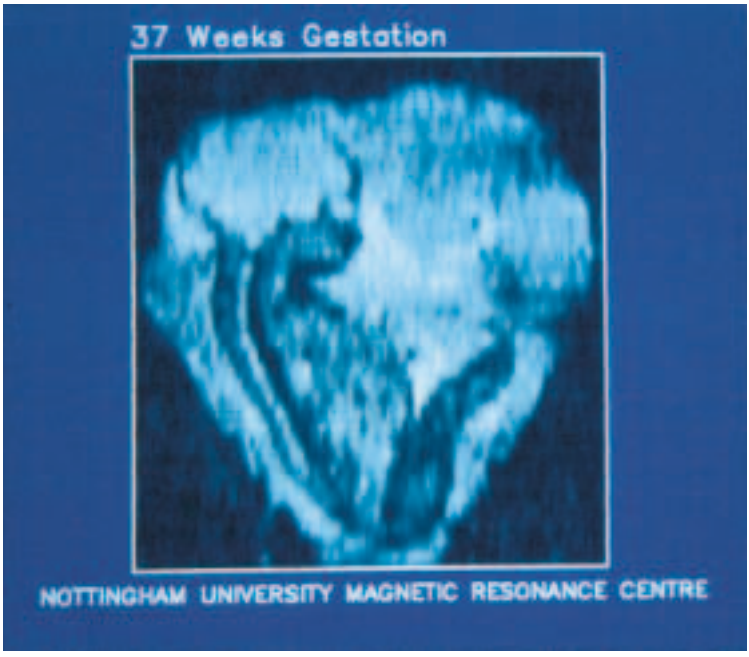

Figure 7. Saggital section taken from a three-dimensional data set of a foetus *in utero* at 37 weeks gestation. The foetal brain and spinal canal can be clearly seen. Also shown to the right and slightly darker is the placenta. The bright region between the placenta and foetus corresponds to amniotic fluid.

(11,12). The foetal volume is assessed from a series of contigious EPI slices spanning the foetus. Using the same technique as described above, the foetal cross-sectional image is traced out and highlighted. The elemental volume is the highlighted area multiplied by the slice thickness. The total foetal volume is then the sum of all cross-sectional slices. The results indicate a good linear correlation between volume and weight.

Paediatric Imaging at 0.5 T

In the course of imaging young children suffering from cyanotic heart disease, (13–16), snap-shot transectional images have been taken through the mediastinum for a child with a normal heart. They all show the lung fields and heart mass at the base of the heart, moving down through the left and right ventricles towards the apex. Also shown is the classification system for a normal heart. This is contrasted with an example taken from a set of images for a child with a truncus arteriosus. Towards the apex the left and right ventricles can be clearly seen as dark regions together with the intact ventricular septum. The left and right atria show as bright regions. The classification diagram indicates the coalescence of the pulmonary artery and the aorta into a common truncus.

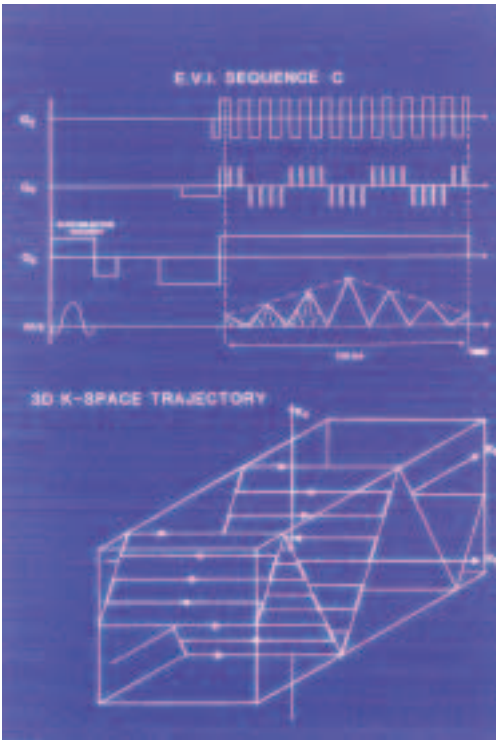

Figure 8. (A) Gradient wave form sequence for (B) (below). T_A = total data acquisition time; T_X = single echo acquisition time; and T_y = a single pulse acquisition time. Dotted portions of G_x and G_y indicate the alternative starting phases. (B) One pass of a general four pass 3D k-space trajectory for EVI. (Reproduced with permission from P R Harvey and P Mansfield, MRM 35:80–88 (1996).)

EPI Results at 3.0 T

A number of snap-shot images of various objects have been obtained at 3.0 T (17), including a snap-shot image of a phantom comprising 256 × 256 pixels. The slice thickness was 0.5 cm. The image acquisition time was approximately 90 ms. Other examples include images through the brain of a normal volunteer. The posterior horns of the ventricles together with part of the anterior horns are just visible in these images.

ECHO-VOLUMAR IMAGING (EVI)

Imaging Sequence

Details of the pulse-timing sequence for EVI (18) are shown in the upper part of Figure 8. The top trace shows the G_y gradient modulation waveform. The next modulated waveform is the gradient G_x. The third waveform G_z includes the slice selection gradient G_z together with a negative pre-positioning pulse immediately followed by a long low level gradient. In the bottom trace the slice selection pulse is indicated and slightly later the modulated spin signals arising from the sequence are sketched.

In the lower half of Figure 8 the k-space trajectory, corresponding to the above described EVI sequence, is sketched. Because of the pre-positioning

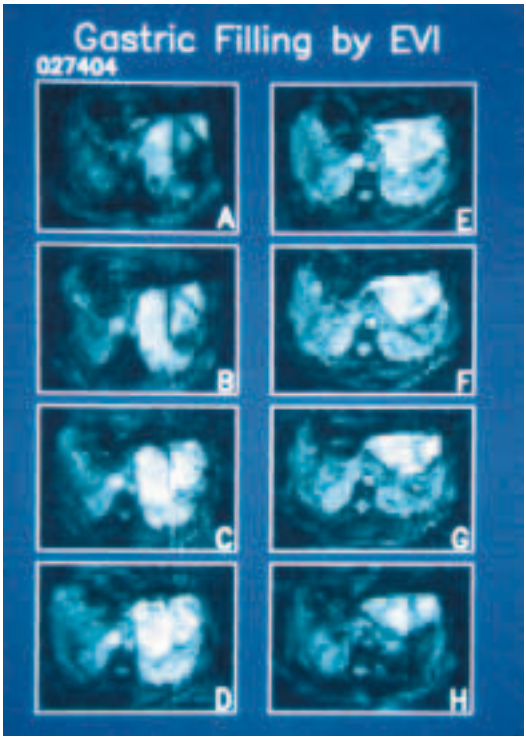

Figure 9. An EVI snap-shot taken from a movie loop showing gastric filling in a volunteer imbibing 1 litre of water. The data set comprises 8 planes spanning approximately an eight cm thick slice through the stomach. The water surface and gaseous void within the stomach are indicated in images (e,f,g). These images correspond approximately to the antrum. Other morphological land marks in these images show the kidneys, liver and spinal canal. (Reproduced with permission from P R Harvey and P Mansfield, MRM 35:80–88 (1996).)

pulse the k-space trajectory starts at $k_x = k_y = 0$ and $k_z = - k_{zmax}$. As shown in the diagram the trajectory moves right to k_{ymax} then to and fro uphill alternately to $\pm k_{ymax}$ until the trace reaches the first peak and k_{xmax}. The trajectory then continues its oscillation as it drops down the negative slope to reach $-k_{xmax}$. The whole process continues uphill and down dale as k_z evolves along the z axis to k_{zmax}.

During the whole process data are sampled (in this case at a constant rate). Because the evolution arrows of the k-trajectory reverse periodically it is necessary to re-order the sampled data so that the arrows are all pointing in the same direction before performing the Fourier transformation to obtain the image. In fact one re-ordering of the k-space data is required producing two slightly different images of the data. However, these maybe combined into a single image with no loss of clarity. Other versions of EVI can also be implemented in which the blips used for G_x are replaced by a square wave modulation of G_x. Even G_z may be replaced by a sequence of blips. However, reasonable quality multi-pass images may be obtained by using square wave modulation of G_x with G_z unmodulated as shown, provided the number of lines in an individual image is large. But these complications can be completely avoided by obtaining one pass snap-shot images using blipped G_x and G_z gradients rather than the square wave or trapezoidally modulated waveform described here.

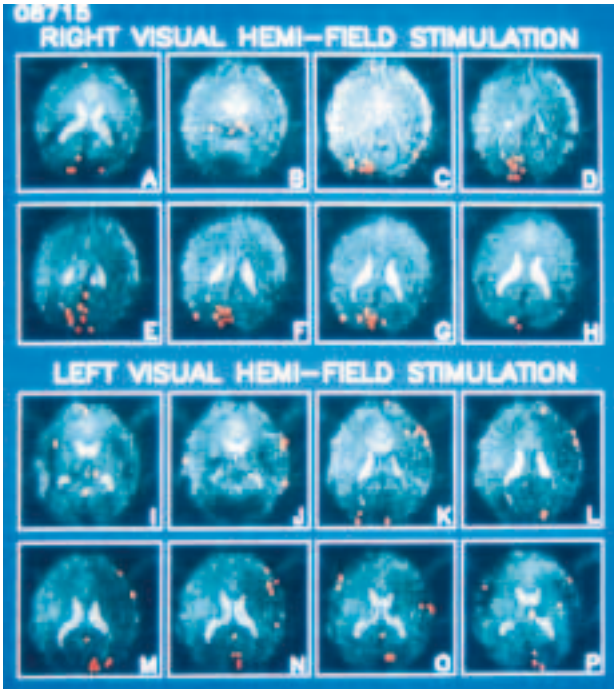

Figure 10. Two complete echo-volumar imaging (EVI) snap shots, each comprising eight contiguous slices. (A–H) One volume set with the functionally active regions highlighted in red corresponding to right visual hemi-field stimulation. (I–P) EVI set 2 shows one volume set with the functionally active regions highlighted in red corresponding to left visual hemi-field stimulation. Transections H and P correspond to the most caudal in each set, respectively. The experimental EVI parameters and resolution details are as follows. Each image comprises 64 × 64 pixels and the slice thickness corresponds to 2.5 mm. (Reproduced with permission from P Mansfield, R Coxon and J Hykin, J CAT 19:847–852 (1995).)

The result of this data manipulation is, in our case, the production of eight simultaneous images. Each image comprises 64 × 64 pixels and each pixel has an in-plane resolution of 6×4 mm^2 and the voxel thickness is 10 mm. The total acquisition time for these eight images is 128 ms. The first EVI images were obtained at 0.5 T with a volunteer subject. The EVI image set shown in Figure 9 shows gastric filling with approximately 1 litre of water (18). The water surface is clearly seen in frames E–H. An EVI snap-shot was also obtained through the bladder of the same volunteer subject. In this case, the images indicate a very full bladder characterized by the very rectangular shape observed (18).

EVI has also been tried at 3.0 T. The first results at this field strength, corresponding to the brain of a normal patient, show the ventricles at slightly different levels (19). The imaging time for all eight cross-sections was 115 ms. In Figure 10 are shown the results of the first EVI functional imaging experiments conducted with a normal volunteer. The upper half of Figure 10 shows eight slices through the brain of a volunteer subjected to right visual hemi-field stimu-

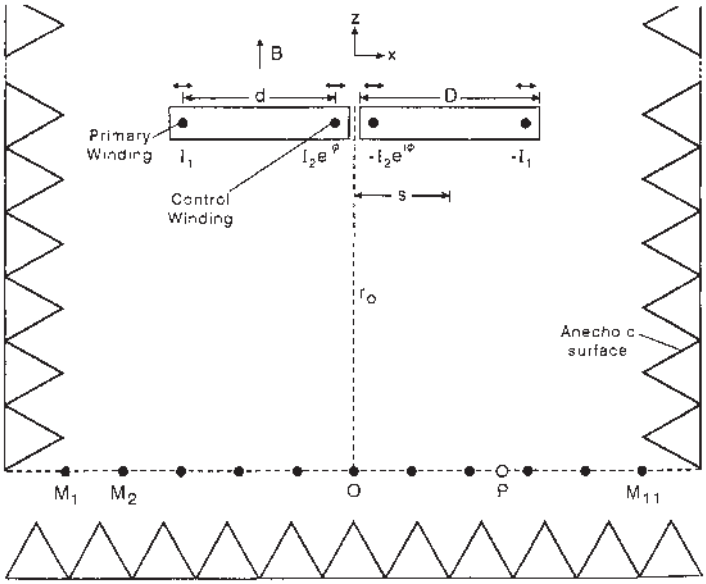

Figure 11. Diagram showing a plan sectional view of a split plate arrangement suspended in an anechoic chamber perpendicular to the main field B (not to scale). Each half of the plate-pair has a width D = 0.126 m. Embedded in each block are two conductors with separation d = 0.1 m. The plate centres are displaced from the assembly origin by ± s = ± 0.063 m. The outer wire pair comprises the primary winding carrying current I_1. The inner wire pair comprises the control winding carrying current $I_2e^{i\varphi}$ where ϕ is the relative phase difference of the two currents. The microphone array lies in a line parallel to the plate through point O. Point P represents a single microphone. The distance r_o = 1.25 m. The plate length I = 0.58 m. The material is GRE, and the plate thickness is 0.012 m. The plate-pair has an overall width of 0.255 m, including an air gap of 0.003 m separating the plates. The compressional wave velocity of sound is taken as 2500 m/s. (Reproduced with permission from B L W Chapman, B Haywood and P Mansfield, MRM 50:931–935 (2003).)

lation. Highlighted on these images are the red dots marking changes in signal arising predominately from the left side of the visual cortex. In the lower eight brain slices the volunteer is subjected to left visual hemi-field stimulation. Also highlighted on these images are red dots marking signal changes in this case arising predominately from the right side of the visual cortex.

ACTIVE ACOUSTIC CONTROL

One of the problems in the implementation of EPI and EVI is the high levels of acoustic noise generated by the gradient coils when pulsed rapidly. The noise originates from movement of the gradient coil windings resulting from the Lorentz forces created by the high currents flowing in the gradient coil assembly. Even if the wires are firmly cemented into the coil former, the former itself deforms slightly and the tiny deformation in the former surface is enough to couple with the surrounding air thereby launching undesirable acoustic waves into and around the MRI apparatus.

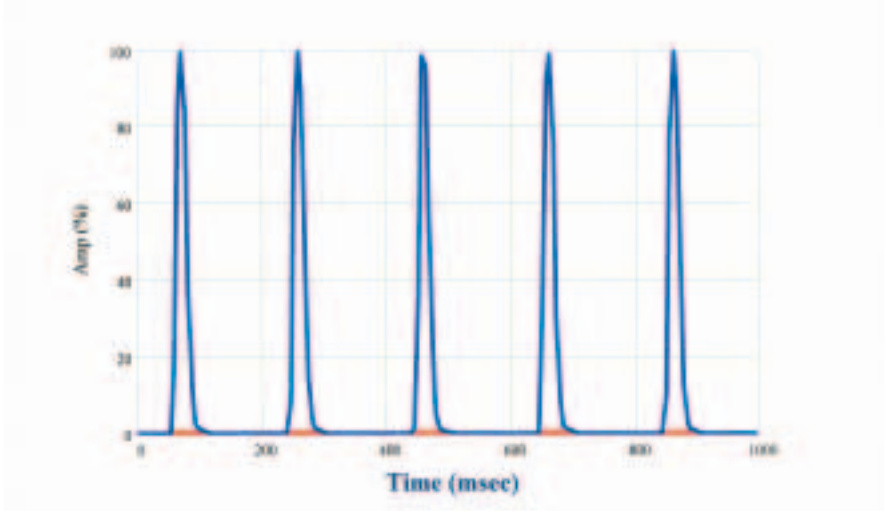

Figure 12. Sound recording before (blue) and during active acoustic control (red) for an optimized gradient pulse sequence running at 5 pulses per second.

The typical noise levels for EPI can reach 140 dB or more. However, the safety levels for noise are limited in the work place to a maximum of 85 dB (20,21). Prolonged exposure to very high level noise can lead to irreversible hearing damage. Of course, some local protection may be introduced to mitigate the effects of high level noise. This often takes the form of ear defenders worn by the patient. These give typically a 30 dB protection. But even these are unreliable for small children because of poor fitting or looseness. For pregnant women there is virtually no reliable protection for the foetus.

It is for these reasons that we have been considering other ways of dealing with the problem. Our current approach is effectively to try to prevent the coil assembly from radiating noise.

Rectangular Gradient Coil

Our initial approach to the acoustic noise problem has been to consider a rather basic coil arrangement comprising four rectangular plates or sectors. Each sector carries a current I_1. In addition there is a re-entrant loop, which constitues the control winding. The control winding current is $I_2e^{i\phi}$ where ϕ is the phase of I_2 relative to I_1. Only one sector so far has been built and tested (22–25).

The test arrangement is shown in Figure 11. The single sector is supported within an anechoic chamber which itself fits into a 3.0 T magnet. A linear array of microphones receives acoustic signals across one end of the magnet.

Theoretical calculations for the acoustic output from a signal sector plate assembly have been performed. These show that when $\phi = 180^\circ$ the plate produces the full acoustic output. This reduces considerably when the phase is adjusted to $\phi = \sim 0^\circ$.

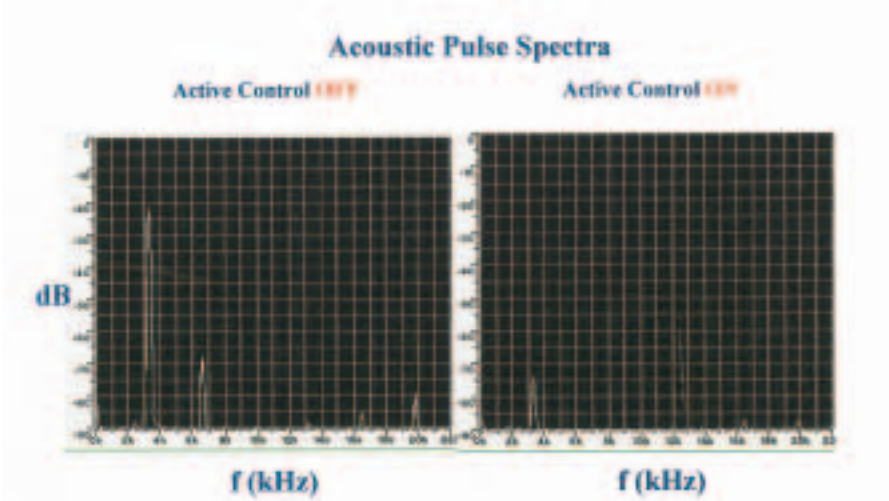

Figure 13. Logarithmic spectra from a 22 m/s Kaiser 7 filtered single pulse with (left) active control off and (right) active control on, showing a resulting reduction in noise of 50 dB (99.7%) in the fundamental noise component at 3.2 kHz. (Reproduced with permission from B L W Chapman, B Haywood and P Mansfield, MRM 50:931–935 (2003).)

Results

A specially designed optimized pulse corresponding to an EPI sequence was used to test the acoustic efficiency of the gradient sector assembly (25). The EPI pulse length was approximately 10 ms. A series of EPI pulses were applied to the gradient sector at a rate of 5 pulses per second in the acoustically optimized mode (red) and non-optimized mode (blue). These results are shown in Figure 12 for five pulses lasting 1 second. The acoustic signal in the optimized mode (red) has been reduced to almost zero level on this linear trace. However, one pulse from the same data has been Fourier analyzed to produce a frequency spectrum of the EPI pulse with and without acoustic control switched on. These results are shown in Figure 13. With active control switched off, acoustic noise of approximately –20 dB occurs primarily at 3.2 kHz, the fundamental carrier frequency of the EPI pulse. Some second harmonic content is present at 6.4 kHz together with higher harmonics. In the optimized mode, the fundamental component of noise is reduced to approximately –70 dB with no second harmonic and reduced higher harmonics. The total noise reduction of the fundamental frequency at 3.2 kHz is 50 dB. Further noise reduction in the harmonic frequencies is also indicated.

CONCLUSIONS

The basis of ultra-high speed snap-shot MRI is reviewed and illustrated with early examples of actual EPI results obtained at 0.5 T and 3.0 T. Also described are some original three dimensional results obtained using snap-shot EVI. Both techniques show promise as useful medical imaging modalities. However it is fair to say that so far only EPI has found its way into regular

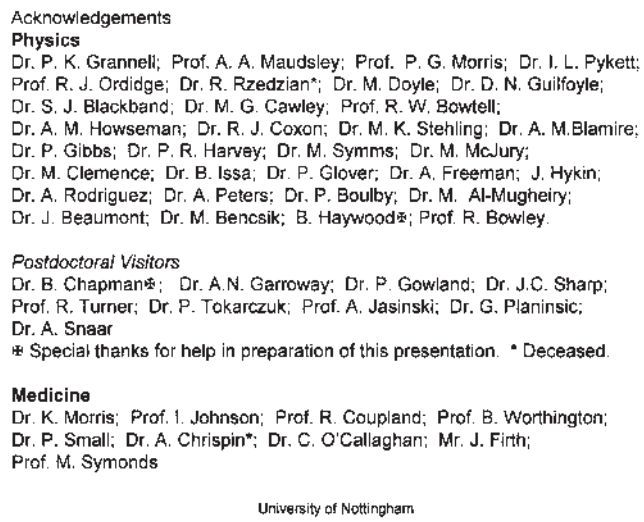

Acknowledgements

Physics

Dr. P. K. Grannell; Prof. A. A. Maudsley; Prof. P. G. Morris; Dr. I. L. Pykett; Prof. R. J. Ordidge; Dr. R. Rzedzian*; Dr. M. Doyle; Dr. D. N. Guilfoyle; Dr. S. J. Blackband; Dr. M. G. Cawley; Prof. R. W. Bowtell; Dr. A. M. Howseman; Dr. R. J. Coxon; Dr. M. K. Stehling; Dr. A. M.Blamire; Dr. P. Gibbs; Dr. P. R. Harvey; Dr. M. Symms; Dr. M. McJury; Dr. M. Clemence; Dr. B. Issa; Dr. P. Glover; Dr. A. Freeman; J. Hykin; Dr. A. Rodriguez; Dr. A. Peters; Dr. P. Boulby; Dr. M. Al-Mugheiry; Dr. J. Beaumont; Dr. M. Bencsik; B. Haywood*; Prof. R. Bowley.

Postdoctoral Visitors

Dr. B. Chapman*; Dr. A.N. Garroway; Dr. P. Gowland; Dr. J.C. Sharp; Prof. R. Turner; Dr. P. Tokarczuk; Prof. A. Jasinski; Dr. G. Planinsic; Dr. A. Snaar

* Special thanks for help in preparation of this presentation. * Deceased.

Medicine

Dr. K. Morris; Prof. I. Johnson; Prof. R. Coupland; Prof. B. Worthington; Dr. P. Small; Dr. A. Chrispin*; Dr. C. O'Callaghan; Mr. J. Firth; Prof. M. Symonds

University of Nottingham

Figure 14. List of past students, post-doctoral assistants and visitors and medical collaborators.

medical use. Quite often this use is limited to a role of rapid sighting of the region of interest within a patient before slower techniques are used to obtain the final image.

The reason for doing things this way round is partly historical. The slower MRI techniques were developed and honed by the manufacturing companies while ignoring the advances in ultra-high speed imaging methods. However, given the same intensive development, EPI and possibly EVI, will move up from a rapid sighting technique to a fully diagnostic technique in its own right.

Such a move would remove the dread felt by some claustrophobic patients at the prospect of being confined in the MRI machine for between a half and one hour. Of course, ultra-high speed imaging brings with it its own problems which need addressing. One of these is the high level of acoustic noise generated by the large and rapidly switched magnetic gradients required for EPI and EVI. Some progress has been made in ameliorating this situation in principle. But it remains to be demonstrated whether the active acoustic control principle can be fully implemented on an operational gradient coil set. For further reading see Refs (26–31).

ACKNOWLEDGEMENTS

I am grateful to my early research supervisors, Professor J G Powles, originally at Queen Mary College, University of London and Professor C P Slichter, at the University of Illinois, Urbana, Illinois, USA for teaching me the art and practice of NMR. I am also greatly indebted to Professor R Bowley and my other colleagues at Nottingham and to my own research students and post-doctoral assistants listed in Figure 14 all of whom contributed extensively to the development of MRI at Nottingham. Also listed are the key medical col-

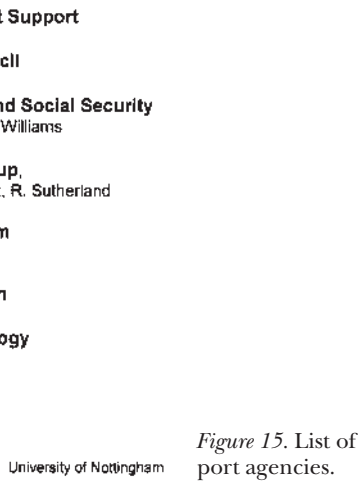

Figure 15. List of funding and equipment support agencies.

leagues whose collaboration and support helped to bring about acceptance of MRI as a diagnostic tool both nationally and internationally.

I am especially grateful to the technical and workshop staff of both the Magnetic Resonance Centre and the Department of Physics and Astronomy for their untiring and unstinting support in the construction and testing of several prototype MRI systems over the years.

I am also most grateful for the financial support received from the Institutions listed in Figure 15. Without their generous and sustained support over many years there would be little to celebrate today.

Finally, I wish to express my sincere appreciation and thanks to my personal secretaries over the years, Mary Newsum-Smith, Lesley Key and most recently, Pamela Davies, for their unflagging efforts in typing and re-typing the many manuscripts, reports and general correspondence.

REFERENCES

1. Multi-pulse line narrowing experiments. P Mansfield, P K Grannell, A N Garroway and D C Stalker, Proc First Specialised Colloque Ampere, Poland (1973).
2. NMR `Diffraction' in solids? P Mansfield and P K Grannell, J Phys C 6, L422 (1973).
3. Image formation in NMR by a selective irradiative process. A N Garroway, P K Grannell and P Mansfield, J Phys C 7, L457, (1974).
4. Medical imaging by NMR. P Mansfield and A A Maudsley, Brit J Radiol 50, 188 (1977).
5. Multi-planar imaging formation using NMR spin echoes. P Mansfield, J Physics C Solid State Phys 10, L55–L58 (1977).
6. Active magnetic screening of coils for static and time-dependent magnetic field generation in NMR imaging. P Mansfield and B Chapman, J Phys E: Sci Instrum 19, 541–546 (1986).
7. Double active magnetic screening of coils in NMR. B Chapman and P Mansfield, J Phys D: Appl Phys 19, L129–L131 (1986).

8. Whole Body Echo-Planar MR Imaging at 0.5 T. M J Stehling, A M Howseman, R J Ordidge, B Chapman, R Turner, R Coxon, P Glover, P Mansfield and R E Coupland, Radiol 170, 257–263 (1989).
9. Ultra-fast magnetic resonance scanning of the liver with echo-planar imaging. M K Stehling, R M Charnley, A M Blamire, R J Ordidge, R Coxon, P Gibbs, J D Hardcastle and P Mansfield, Brit J of Radiol, 63, 430–437 (1990).
10. Estimation of lung volume in infants by echo planar imaging and total body plethysmography. B Chapman, C O'Callaghan, R J Coxon, P M Glover, G Jaroszkiewicz, A M Howseman, P Mansfield, P Small, A D Milner and R E Coupland, Arch Dis in Childhood 65, 168–170 (1990).
11. Fetal weight estimation by echo-planar magnetic resonance imaging. P N Baker, I R Johnson, P A Gowland, J Hykin, P R Harvey, A Freeman, V Adams, B S Worthington, P Mansfield, Lancet 343, 644–45 (1994).
12. Obstetrics. Echo-planar magnetic resonance imaging in the estimation of fetal weight. J Hykin, P Gowland and P Mansfield, Contemp Rev Obstet Gynaecol 6, 173–177 (1994).
13. Transectional echo planar imaging of the heart in cyanotic congenital heart disease. A Chrispin, P Small, N Rutter, R E Coupland, M Doyle, B Chapman, R Coxon, D Guilfoyle, M Cawley and P Mansfield, Pediatr Radiol 16, 293–297 (1986).
14. Echo-planar imaging of normal and abnormal connections of the heart and great arteries. A Chrispin, P Small, N Rutter, R E Coupland, M Doyle, B Chapman, R Coxon, D Guilfoyle, M Cawley and P Mansfield, Pediatr Radiol 16, 289–292 (1986).
15. EPI of the infant heart (1). Demonstration of connection between ventricle and artery by EPI construction. P Mansfield with P Small, A Chrispin, N Rutter, R E Coupland, M Doyle, B Chapman, D N Guilfoyle and M G Cawley, Paediatric Radiol 15, 280 (1985).
16. EPI of the infant heart (2). Demonstration of ventriculo/bulbar septation by EPI transection. P Mansfield with A Chrispin, P Small, N Rutter, R E Coupland, M Doyle, B Chapman, D N Guilfoyle and M G Cawley, Paediatric Radiol 15, 280 (1985).
17. Echo-Planar Imaging of the Brain at 3.0 T: First Normal Volunteer Results. P Mansfield, R Coxon and P Glover, J CAT, 18(3): 339–343 (1994).
18. Echo-Volumar Imaging (EVI) at 0.5 T: First Whole-Body Volunteer Studies. P R Harvey and P Mansfield, Mag Res Med 35, 80–88 (1996).
19. Echo-Volumar Imaging (EVI) of the Brain at 3.0 T: First Normal Volunteer and Functional Imaging Results. P Mansfield, R Coxon and J Hykin, J CAT 19(6): 847–852 (1995).
20. NRPB Board Statement on Clinical MR Diagnostic Procedures, 2:1 (1991).
21. Price RR The AAPM/RSNA physics tutorial for residents: MR imaging safety considerations. Radiographics 19, 1641-1651 (1999).
22. Sound Generation in Gradient Coil Structures for MRI. P Mansfield, P M Glover and J Beaumont, Mag Res Med 39, 539–550 (1998).
23. Principles of Active Acoustic Control in Gradient Coil Design. P Mansfield and B Haywood, Magma 10, 147–151 (2000).
24. Active Acoustic Control in Gradient Coils for MRI. P Mansfield, B Haywood and R Coxon, Mag Red Med 46, 807–818 (2001).
25. Optimized Gradient Pulse for Use with EPI Employing Active Acoustic Control. B L W Chapman, B Haywood and P Mansfield, Mag Res Med 50, 931–935 (2003).
26. Snapshot echo-planar imaging methods: current trends and future perspectives. P Mansfield, A M Blamire, R Coxon, P Gibbs, D N Guilfoyle, P Harvey and M Symms, Phil Trans. R. Soc. Lond. A 333, 495–506 (1990).
27. Snapshot Imaging at 0.5 T Using Echo-Planar Techniques. R Ordidge, A Howseman, R Coxon, R Turner, B Chapman, P Glover, M Stehling and P Mansfield, Mag Res Med 10, 227–240 (1989).
28. Echo-Planar Imaging: Magnetic Resonance Imaging in a Fraction of a Second. M K Stehling, R Turner and P Mansfield, Science 254, 43–50 (1991).
29. 'N.M.R. Imaging in Biomedicine', P Mansfield and P G Morris, Academic Press, New York, (1982).

30. ‘Echo-Planar Imaging: Theory, Technique and Application’. F Schmitt, M K Stehling and R Turner, Springer-Verlag, Heidelberg, (1998).
31. ‘NMR Imaging in Medicine and Biology’. P G Morris, Clarendon Press, Oxford (1986).